Constraining the baryonic feedback with cosmic shear using the DES Year-3 small-scale measurements

A. Chen [1,2]* G. Aricò,[3,4,5]* D. Huterer,[1] R. E. Angulo,[4,6] N. Weaverdyck,[1,7] O. Friedrich,[8] L. F. Secco,[9]
C. Hernández-Monteagudo,[10,11] A. Alarcon,[12] O. Alves,[1,13] A. Amon,[14] F. Andrade-Oliveira,[1] E. Baxter,[15]
K. Bechtol,[16] M. R. Becker,[12] G. M. Bernstein,[17] J. Blazek,[18,19] A. Brandao-Souza,[13,20] S. L. Bridle,[21]
H. Camacho,[13,22] A. Campos,[23] A. Carnero Rosell,[13,24,25] M. Carrasco Kind,[26,27] R. Cawthon,[28]
C. Chang,[9,29] R. Chen,[30] P. Chintalapati,[31] A. Choi,[32,33] J. Cordero,[21] M. Crocce,[34,35] M. E. S. Pereira,[36]
C. Davis,[14] J. DeRose,[7] E. Di Valentino,[21] H. T. Diehl,[31] S. Dodelson,[23,37] C. Doux,[17,38]
A. Drlica-Wagner,[9,29,31] K. Eckert,[17] T. F. Eifler,[39,40] F. Elsner,[41] J. Elvin-Poole,[42,43] S. Everett,[40]
X. Fang,[39,44] A. Ferté,[40] P. Fosalba,[34,35] M. Gatti,[17] E. Gaztanaga,[34,35] G. Giannini,[45] D. Gruen,[46]
R. A. Gruendl,[26,27] I. Harrison,[21,47,48] W. G. Hartley,[49] K. Herner,[39] K. Hoffmann,[3] H. Huang,[39,50]
E. M. Huff,[40] B. Jain,[17] M. Jarvis,[17] N. Jeffrey,[41,51] T. Kacprzak,[52] E. Krause,[39] N. Kuropatkin,[31]
P.-F. Leget,[14] P. Lemos,[41,53] A. R. Liddle,[54] N. MacCrann,[55] J. McCullough,[14] J. Muir,[56] J. Myles,[14,57,58]
A. Navarro-Alsina,[20] Y. Omori,[9,14,29,57] S. Pandey,[17] Y. Park,[2] A. Porredon,[42,43] J. Prat,[9,29] M. Raveri,[17]
A. Refregier,[52] R. P. Rollins,[21] A. Roodman,[14,58] R. Rosenfeld,[13,59] A. J. Ross,[42] E. S. Rykoff,[14,58]
S. Samuroff,[23] C. Sánchez,[17] J. Sanchez,[31] I. Sevilla-Noarbe,[60] E. Sheldon,[61] T. Shin,[62] A. Troja,[13,59]
M. A. Troxel,[30] I. Tutusaus,[34,35,63] T. N. Varga,[64,65,66] R. H. Wechsler,[14,57,58] B. Yanny,[31] B. Yin,[23]
Y. Zhang,[67] J. Zuntz,[68] M. Aguena,[13] J. Annis,[31] D. Bacon,[69] E. Bertin,[70,71] S. Bocquet,[46] D. Brooks,[41]
D. L. Burke,[14,58] J. Carretero,[45] C. Conselice,[21,72] M. Costanzi,[73,74,75] L. N. da Costa,[13] J. De Vicente,[60]
S. Desai,[76] P. Doel,[41] I. Ferrero,[77] B. Flaugher,[31] J. Frieman,[9,31] J. García-Bellido,[78] D. W. Gerdes,[1,79]
T. Giannantonio,[8,80] J. Gschwend,[13,81] G. Gutierrez,[31] S. R. Hinton,[82] D. L. Hollowood,[83]
K. Honscheid,[42,43] D. J. James,[84] K. Kuehn,[85,86] O. Lahav,[41] M. March,[17] J. L. Marshall,[67] P. Melchior,[87]
F. Menanteau,[26,27] R. Miquel,[45,88] J. J. Mohr,[46,65] R. Morgan,[16] F. Paz-Chinchón,[26,80] A. Pieres,[13,81]
E. Sanchez,[60] M. Smith,[89] E. Suchyta,[90] M. E. C. Swanson,[1] G. Tarle,[1] D. Thomas,[69] and C. To[42]
(DES Collaboration)

Affiliations are listed at the end of the paper

ABSTRACT

We use the small scales of the Dark Energy Survey (DES) Year-3 cosmic shear measurements, which are excluded from the DES Year-3 cosmological analysis, to constrain the baryonic feedback. To model the baryonic feedback, we adopt a baryonic correction model and use the numerical package BACCOEMU to accelerate the evaluation of the baryonic non-linear matter power spectrum. We design our analysis pipeline to focus on the constraints of the baryonic suppression effects, utilizing the implication given by a principal component analysis on the Fisher forecasts. Our constraint on the baryonic effects can then be used to better model and ameliorate the effects of baryons in producing cosmological constraints from the next-generation large-scale structure surveys. We detect the baryonic suppression on the cosmic shear measurements with a $\sim 2\sigma$ significance. The characteristic halo mass for which half of the gas is ejected by baryonic feedback is constrained to be $M_c > 10^{13.2} \, h^{-1} \, M_\odot$ (95 per cent C.L.). The best-fitting baryonic suppression is ~ 5 per cent at $k = 1.0 \, \mathrm{Mpc} \, h^{-1}$ and ~ 15 per cent at $k = 5.0 \, \mathrm{Mpc} \, h^{-1}$. Our findings are robust with respect to the assumptions about the cosmological parameters, specifics of the baryonic model, and intrinsic alignments.

Key words: gravitational lensing: weak – large-scale structure of Universe – cosmology: observations.

---

* E-mail: anqi.chen@ipmu.jp (AC); arico.giovanni.92@gmail.com (GA)

1 INTRODUCTION

Baryons impact the density profiles of dark-matter-dominated cosmic structures on small spatial scales. As a consequence, they also affect the total-matter clustering signal. We call such baryonic physics impact on the total-matter clustering 'baryonic feedback', incorporating many possible mechanisms like active galactic nuclei (AGNs), gas cooling, metallicity evolution, etc. In most of the cases, AGN is the most important mechanism at the scale relevant to the large-scale structure surveys, and it would lower the matter power by throwing a part of the baryonic matters out of the galaxy. While the effects of baryons are most noticeable in the clustering signal within individual haloes, they extend out to the two-halo regime, on scales corresponding to a few megaparsecs. These effects thus complicate the cosmological inferences from surveys mapping out the clustering of cosmic structures. In order to mitigate this uncertainty in the cosmological analyses in the coming generation of large-scale structure surveys, considerable effort has been undertaken to build reliable predictions for the baryonic feedback, including the adoption of the halo model (Mead et al. 2021), principal component analysis on the baryonic suppression modes (Huang et al. 2019), and calibrated simulations (Schneider & Teyssier 2015; Aricò et al. 2020). In parallel, a growing number of analyses have been dedicated to assessing and validating these baryonic-modelling approaches (MacCrann et al. 2016; Huang et al. 2021; Gatti et al. 2022a; Lee et al. 2022; Nicola et al. 2022; Thiele et al. 2022; Tröster et al. 2022; Schneider et al. 2022).

While the impact of baryons can be modelled with hydrodynamical *N*-body simulations (Schaye et al. 2010, 2015; Le Brun et al. 2014; McCarthy et al. 2017; Springel et al. 2018), these results typically depend on the physics adopted in the simulations. Thus the inferred baryonic feedback depends on the values of free parameters, which are in turn determined by a sub-grid recipe for baryonic physics. Because the hydrodynamical simulations are computationally very demanding, rerunning them for many baryonic scenarios quickly becomes prohibitive. Therefore, accurate yet efficient modelling of the effect of baryons on clustering remains a key challenge in cosmology. Addressing and solving this challenge will be required for upcoming surveys such as Euclid (Martinelli et al. 2021), the Rubin and Roman telescopes (Eifler et al. 2021), the Dark Energy Spectroscopic Instrument (DESI) (Fagrelius 2020), and Subaru Prime Focus Spectrograph (Takada et al. 2014).

'Baryonification' (Schneider & Teyssier 2015; Aricò et al. 2020) is one such method that enables an efficient yet accurate modelling of the effects of baryons. This approach is based on the fundamental premise that the baryonic effects can be captured by shifting the position of particles in gravity-only *N*-body simulations. The shift is computed by means of parametrizing the difference between density profiles of cosmic structures with and without baryons. This introduces a few physically motivated free parameters which can be constrained with observations or hydrodynamical simulations.

Our goal here is to apply the baryonification modelling to the data utilized in the Year-3 analysis of the Dark Energy Survey (DES) (Sheldon et al. 2020; Gatti et al. 2021, 2022b; Sevilla-Noarbe et al. 2021). These observations have a footprint of nearly 5000 square deg on the sky, and comprise the redshift and shape measurements of over 100 million galaxies, with the mean redshift $z = 0.63$ (Secco et al. 2022). In principle, all of the key observations that comprise the '3x2pt' DES Y3 analysis (Abbott et al. 2022) – galaxy clustering, galaxy–galaxy lensing, and cosmic shear – would benefit from the baryonification analysis, as all three extend to scales potentially affected by baryons. In this paper, however, we only consider the

DES Y3 observations of cosmic shear (Amon et al. 2022; Secco et al. 2022). We leave the application of baryonification to the full 3x2pt analysis to future work, because systematics other than the baryonic effect, for example the galaxy bias, are more predominant for the galaxy clustering and galaxy–galaxy lensing analysis.

A model dedicated to describe the baryonic effect on the large-scale structure typically adds one or more free parameters to the cosmological parameter space, while enabling the extension of the clustering constraints to smaller scales. In this work, among the first several adoptions of the baryonification model for a wide-field galaxy survey, we do a simpler analysis in order to study the effectiveness of this approach. We fix the cosmological parameters to the best-fitting model derived in the standard analysis, then *only* utilize the scales smaller than those used in the standard analysis in order to constrain the baryonification parameter(s). Therefore, instead of focusing on the cosmological parameters, we instead study the baryonic physics, measuring the amount of baryonic feedback in structure formation. The results obtained in this type of analysis can subsequently serve to provide a prior for the modelling of baryons in upcoming surveys, and thus help maximize the cosmological information from ongoing and future surveys such as DESI, Euclid, Rubin and Roman observatories, Hyper-Suprime Camera Survey (HSC), and Spherex.

The paper is organized as follows. In Section 2, we describe the baryonification method and the corresponding numerical tools that we use. In Section 3, we describe our analysis, and in Section 4 we present its results. In Section 5, we discuss the results, and compare them to others in the literature. We conclude in Section 6. Additional information about our methods, results, and comparisons is available in the Appendices.

2 METHODOLOGY

We model the matter power spectrum employing a series of Neural Network emulators from the BACCO Simulation project (Angulo et al. 2021) (BACCOEMU). Specifically, the matter power spectrum is decomposed in three different components: a linear part given by perturbation theory, a non-linear boost function, and a baryonic correction. The linear component is a direct emulation of the Boltzmann solver CLASS (Lesgourgues 2011); it speeds up the calculations by several orders of magnitude while introducing a negligible error (Aricò, Angulo & Zennaro 2021a). The non-linear boost function is built by interpolating the output of more than 800 simulations, obtained by scaling the cosmologies of six high-resolution *N*-body simulations of $\approx$2Gpc and 4320^3 particles, using the methodology developed in Angulo & White (2010), Zennaro et al. (2019), Contreras et al. (2020), and Angulo et al. (2021). This algorithm manipulates a given simulation snapshot to mimic the expected particle distribution in a cosmological space that spans roughly the 10σ region around Planck 2018 best fits (Planck Collaboration VI 2020). The parameter space includes dynamical dark energy and massive neutrinos, and models the power spectrum with an accuracy of 2–3 per cent (Contreras et al. 2020; Angulo et al. 2021). Finally, the baryonic correction is computed applying a baryonification algorithm (Schneider & Teyssier 2015; Aricò et al. 2020) to the *N*-body simulations. The baryonification, or Baryon Correction Model (BCM), displaces the particles in a gravity-only simulation according to theoretically motivated analytical corrections (Schneider & Teyssier 2015; Aricò et al. 2020) to model the impact of baryons on the density field. In the BCM framework, haloes are assumed to be made up of galaxies, gas in hydrostatic equilibrium, and dark matter. A given fraction of the gas is expelled from the haloes by accreting supermassive black holes, and the

dark matter backreacts on the baryon gravitational potential with a quasi-adiabatic relaxation. The model employed has seven physically motivated free parameters, although we will show that varying just one parameter will be sufficient for our purposes. We refer the reader to Appendix A for further details on the baryonification. By working at the field level, the BCM can provide predictions on multiple observable quantities, e.g. clusters' gas fraction from X-ray or kinetic Sunyaev–Zeldovich effect (Giri & Schneider 2021; Schneider et al. 2021). Moreover, the BCM has proven flexible enough to reproduce the two-point and three-point statistics of several hydrodynamical simulations (Aricò et al. 2021b). The emulator that we employ fully captures the degeneracies between baryonic and cosmological parameters, while being accurate at several per cent level (Aricò et al. 2021c).

Having emulated the non-linear matter power spectrum with baryonic effects modelled by BACCOEMU, we follow the same methodology as described in section IV.B in Secco et al. (2022) to model the tomographic weak lensing two-point correlation functions. We are projecting the 3D matter power spectrum into 2D angular-space correlation functions, using the lensing kernel from the redshift-binned source galaxy samples. Hence we expect the baryonic suppression at small scales in the matter power spectrum to be reflected in the tomographic 2pt functions.

3 ANALYSIS CHOICES

Our goal is to constrain the baryonic feedback using the DES Year-3 measurements of cosmic shear tomographic two-point correlation functions (Amon et al. 2022; Secco et al. 2022) measured at small scales that were discarded in the standard cosmological analysis. We start with a Fisher forecast in Section 3.1 to inform how to reduce the dimensionality of the parameter space in the analysis. Then we specify the parameter priors and the nested sampling pipeline of our analysis in Sections 3.2 and 3.3. We discuss the possible systematics that could affect the baryonic feedback constraints in Section 3.4, and at the end we finalize the blinding scheme in Section 3.5 based on the considerations in this section. The real-data analysis pipeline is identical to the synthetic-data tests described in this section; the only difference is of course that fake data are replaced by real observations.

3.1 Principal component analysis on Fisher forecasts

The first choice to make in our analysis is to determine the baryonic parameter space that is sensitive to the precision of the measurements currently available to us. As recapped in Appendix A, there are seven parameters introduced by the baryonic correction model adopted by BACCOEMU. With the signal to noise of the small-scale cosmic shear measurements only, we are not likely to be able to constrain all of them. Additionally, these unconstrained extra parameters can exacerbate convergence problems during the Monte Carlo sampling. We therefore need a strategy to identify the subset of new parameters that are relevant to vary when analysing an extended theoretical model, given the limited precision of data we have in hand.

We introduce our innovative parameter space compression strategy as follows. We define a metric $\mathcal{R}_{\mathrm{FoM}} \leq 1$ to quantify how well a multidimensional hypercube spanned by a subset of the parameters overlaps with the sub-parameter space best constrained by the data:

$$\mathcal{R}_{\mathrm{FoM}}(\boldsymbol{\theta}) = \mathrm{FoM}_{\boldsymbol{\theta}} \Bigg/ \prod_{i=1}^{N_{\boldsymbol{\theta}}} \sqrt{\lambda_i} \, , \qquad (1)$$

where $\boldsymbol{\theta}$ is a subset of model parameters, $N_{\boldsymbol{\theta}}$ is the number of the parameters in this subset, λ_i are the eigenvalues of the Fisher matrix in the decreasing order, and

$$\mathrm{FoM}_{\boldsymbol{\theta}} = 1/\sqrt{\det\left[(\mathcal{F}^{-1})|_{\boldsymbol{\theta}}\right]}. \qquad (2)$$

Here, we take the submatrix corresponding to $\boldsymbol{\theta}$ from the full Fisher matrix inverse to calculate the determinants.

We use two criteria to aid the identification of the parameters $\boldsymbol{\theta}$ that are sensitive to the data:

(i) **Criterion I**: $\mathcal{R}_{\mathrm{FoM}}(\boldsymbol{\theta}) \approx 1$. When $\mathcal{R}_{\mathrm{FoM}}(\boldsymbol{\theta})$ approaches 1 from below, then the multidimensional hypercube spanned by $\boldsymbol{\theta}$ – a subset of the model parameters – overlaps with the space constrained by the first $N_{\boldsymbol{\theta}}$ principal components.

(ii) **Criterion II**: $\prod_{i=1}^{N_{\boldsymbol{\theta}}} \sqrt{\lambda_i} / \prod_{i=1}^{N} \sqrt{\lambda_i} \approx 1$, where λ_i are normalized to 1 for unconstrained (prior-dominated) principal components. This gives a measure of how much total information gain *over the prior* is contained within just the first $N_{\boldsymbol{\theta}}$ principal components.

Both quantities featured in these two criteria are ≤ 1. When they approach unity simultaneously, then we can declare that the parameters not contained in $\boldsymbol{\theta}$ are insensitive to the data. We can thus justifiably vary $\boldsymbol{\theta}$ and fix all other parameters in the analysis.

Note that this whole argument is predicated on the assumption of a Gaussian posterior, which the Fisher matrix formalism assumes from the beginning.

In our scenario of modelling the small scales of cosmic shear by introducing the BCM parameters, we first carry out the Fisher matrix calculation using the FISHER routine of the COSMOSIS software. The Fisher matrix is defined as

$$\mathcal{F}_{ij} = \sum_{mn} \frac{\partial v_m}{\partial p_i} \left[C^{-1}\right]_{mn} \frac{\partial v_n}{\partial p_j} + \left[\mathcal{I}^{-1}\right]_{ij} . \qquad (3)$$

Here, v_{m} are the measured data points which are organized in a *data vector*, p_i are the model parameters, and C is the measurement covariance matrix. Next, $\mathcal{I}_{ij}$ is the prior term, which is typically a diagonal matrix with elements $1/\sigma_i^2$ for uncorrelated priors, where σ_i is the variance of the Gaussian prior of the i-th parameter. [For parameters on which we apply *flat* priors, we calculate the equivalent Gaussian priors $\sigma_i \mathrm{d}$, whose Gaussian variance scales with the flat prior range.] When $\mathcal{F}_{ij}$ approaches $\mathcal{I}_{ij}$, the data are not providing information to the model parameters, and their constraints are dominated by the priors.

In the Fisher forecast, we vary the six cosmological parameters, 13 DES nuisance parameters, and seven baryonic parameters; see Table 1. The six cosmological parameters that we vary are matter and baryon densities relative to critical Ω_{m} and Ω_{b}, amplitude of mass fluctuations σ_8, scaled Hubble constant h, and the (physical) neutrino density $\Omega_\nu h^2$. The detailed definitions of the 13 nuisance parameters (listed in Table 1 as intrinsic alignment, source photo-z shift, and shear calibration parameters) are given in Secco et al. (2022), while the baryonic parameters are fully defined in Aricò et al. (2021b). Note also that the characteristic masses, for example the halo mass scale that contains half of the total gas, M_c, are defined in units of $h^{-1}\,\mathrm{M}_\odot$. This gives us a Fisher matrix with a total of 26 parameters.

We marginalize over all of the 13 DES nuisance parameters, as well as the three cosmological parameters h, n_s, and the sum of neutrino mass M_ν, by dropping them from the inverse Fisher matrix. We do so because cosmic shear measurements, which we are adopting here, are known to be rather insensitive to all of these parameters.

We then diagonalize the Fisher matrix in the remaining 10 parameters to find the principal components in this final parameter

Table 1. Cosmological and nuisance parameters in our DES-Y3 small-scale cosmic shear analysis, and their priors. The 'DES-Y3 3x2pt covariance' label for Ω_m and σ_8 prior means that the posterior in this 2D parameters plane obtained from DES Y3 3x2pt analysis is applied as prior in our analysis (see the red contour in Fig. 5). Our other cosmological parameters are fixed to the Planck best-fitting values, and other BCM parameters are fixed to the best fit to OWLS-AGN hydrodynamic simulations. The nuisance parameter priors (IA, photo-z shifts, and shear calibrations) are the same as DES Year-3 cosmic shear cosmological analysis.

Parameter	Prior
Cosmological	
Ω_m	$\in [0.23, 0.4]$, DES-Y3 3x2pt covariance
σ_8	$\in [0.73, 0.9]$, DES-Y3 3x2pt covariance
h	0.6727
Ω_b	0.0493
n_s	0.9649
$\Omega_\nu h_0^2$	0.00083
Intrinsic Alignment	
TATT model	
$A_{1, IA}$	flat $(-5, 5)$
$\alpha_{1, IA}$	flat $(-5, 5)$
$A_{2, IA}$	flat $(-5, 5)$
$\alpha_{2, IA}$	flat $(-5, 5)$
b_{ta}	flat $(0, 2)$
Source photo-z shift	
Δz_s^1	Gauss $(0.0, 0.018)$
Δz_s^2	Gauss $(0.0, 0.015)$
Δz_s^3	Gauss $(0.0, 0.011)$
Δz_s^4	Gauss $(0.0, 0.017)$
Shear calibration	
m_1	Gauss $(-0.0063, 0.0091)$
m_2	Gauss $(-0.0198, 0.0078)$
m_3	Gauss $(-0.0241, 0.0076)$
m_4	Gauss $(-0.0369, 0.0076)$
BCM parameters	
$\log \theta_{out}$	0.419
$\log \theta_{inn}$	-0.702
$\log \eta_b$	-0.248
$\log \beta_b$	0.321
$\log M_{inn}$	13.0
$\log M_c$	flat $(12.0, 15.0)$
$\log(M_{z0,cen})$	10.4

space, which consists of the baryonic parameters and the cosmological parameters of interest, Ω_b, Ω_m, σ_8. Let us denote the eigenvalues in this 10D space, in descending order, as λ_i, $i = 1...10$, and the (normalized) principal components – the eigenvectors – as $p_i^{\theta_j}$.

Fig. 1 shows a colour map in this 10D parameter space. The colour is proportional to the quantities $|p_i^{\theta_j} \times \sqrt{\lambda_i}|$, where $p_i^{\theta_j}$ is the coefficient of parameter θ_j in the principal component PC_i. These quantities combine the PCs' weights – their eigenvalues – with the coefficients of the parameters within that PC, to give an overall indication of how well the parameter is constrained by the data. For example, $\log(M_c)$ has the largest coefficients of all parameters within the first (best-constrained) principal component, and can thus be reasonably expected to be the best-constrained single parameter in the full analysis. The first two principal components are dominated by $\log(M_c)$, Ω_m, and σ_8, indicating that these parameters are the best constrained by our data.

Next, we quantitatively check the two criteria we proposed above to investigate whether these three parameters are the only parameters
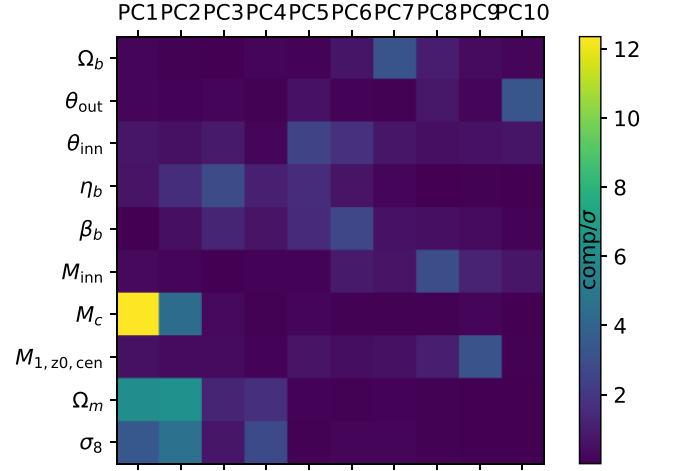

Figure 1. Colour map of the value $|p_i^{\theta_j} * \sqrt{\lambda_i}|$, where $p_i^{\theta_j}$ is the coefficient of parameter θ_j in the principal component PC_i, and λ_i is the eigenvalue of PC_i for the 10-dimensional Fisher matrix. The Fisher matrix is calculated in the full parameter space with DES Year-3 small-scale cosmic shear synthesized data vector, and is marginalized over the nuisance parameters and the unconstrained parameters h, n_s, and M_ν; see the text for details.

constrained by the data instead of the priors. For the three-parameter subspace $(\log(M_c), \Omega_m, \sigma_8)$, Criterion I evaluates to

$$\mathcal{R}_{\text{FoM}}(\log(M_c), \Omega_m, \sigma_8) = \frac{\text{FoM}_{\log(M_c), \Omega_m, \sigma_8}}{\prod_{i=1}^3 \sqrt{\lambda_i}}$$
$$= 0.836. \tag{4}$$

In other words, when we choose to utilize three degrees of freedom to describe the constrained parameter space, the choice of the physically meaningful parameters $\log(M_c)$, Ω_m, and σ_8 can reproduce 83.6 per cent of the Figure of Merit of the more optimal but less interpretable choice of the first three principal components.

For the Criterion II, when we normalize eigenvalues to $\lambda_i = 1$ for prior only principal components, we find

$$\prod_{i=1}^3 \sqrt{\lambda_i} \bigg/ \prod_{i=1}^{10} \sqrt{\lambda_i} = 0.975 . \tag{5}$$

This indicates that the PCs beyond the first three (so fourth, fifth, etc. PC) are almost fully prior dominated. Hence, we conclude that the constrained parameter space for our small-scale cosmic shear analysis is almost completely spanned by the three parameters $\log(M_c)$, Ω_m, and σ_8, and we can fix the other cosmological and baryonic parameters.

The parameter M_c is defined in Aricò et al. (2021b) as the halo mass scale that contains half of the total gas. In the same reference, they demonstrate that, among the seven BCM parameters, the baryon feedback suppression $S(k) = P_{\text{BCM}}(k)/P_{\text{DMO}}$ responds to the variation of M_c most significantly; this agrees with our Fisher-forecast conclusions. Hence, in our real-data analysis, varying $\log(M_c)$ alone is analogous to measuring the amplitude of a specific pattern of baryon feedback, whose redshift and wavenumber dependence are motivated by theory and simulations. The priors on $\log(M_c)$ and other fixed BCM parameters will be presented in the next subsection.

In conclusion, the Fisher PCA approach that we just described enabled us to determine the baryonic parameter space that can be constrained by the DES Y3 measurements.

3.2 Priors

To get the best constraining power on the parameters that the small-scale cosmic shear analysis is sensitive to ($\log(M_c)$, Ω_m, and σ_8), we fix the other cosmological and baryonic parameters to the values based on best available information. We give the fixed cosmological parameters the mean values reported in the Planck-2018 TTTEEE + lowEE analysis (Planck Collaboration VI 2020). To the baryonic parameters other than $\log(M_c)$, we assign the values inferred from the power spectrum produced by the OWLS-AGN simulation at redshift $z = 0$ (Schaye et al. 2010); see Table 1. In the spirit of utilizing the available cosmological information to focus our constraining power on the baryonic parameters, we further apply the posterior in the $\Omega_m - \sigma_8$ space from the DES-Y3 3x2pt Λ cold dark matter analysis as a part of our prior; we henceforth refer to this as the DES-Y3 prior. This prior, Gaussian but correlated in Ω_m and σ_8, captures information provided by large-scale analysis of weak lensing, galaxy clustering, and galaxy–galaxy lensing. Because BACCOEMU is trained around the best fit of Planck cosmology, and there is a well-known $\sim 2\sigma$ downward shift in the late-Universe σ_8 measurement compared to Planck, BACCOEMU range covers only a half of our σ_8 prior at the higher value end, as illustrated in Fig. 5. It is possible to cause some projection effect, which we leave to be taken care of in the future work, with an updated version of BACCOEMU trained in larger spaces.

3.3 Pipeline

We use BACCOEMU[1] (Aricò et al. 2021b) to emulate the linear and non-linear matter power spectrum with baryonic effects, as described in Section 2. The maximum wavenumber encoded by the emulator goes up to $k = 5.0$, and beyond this scale we linearly extrapolate the logarithm of the matter power spectrum to high-k for 2D projection purpose. We use the data vector of cosmic shear measurements in configuration space, $\xi_\pm$, only at small scales. Namely, we use the same scale cuts as the fiducial DES Year-3 cosmic shear analysis, but in the opposite way, adopting only the data points at angles smaller than the scale cuts. Because DES cosmic shear scale cuts are determined by minimizing the effects of baryonic feedback (Amon et al. 2022; Secco et al. 2022), adopting the complementary scale cuts lets us utilize the data that are the most sensitive to the baryonic feedback. With this removal of the large scales used in the cosmology analysis adopted, we have 173 data points (measurements of $\xi_\pm$). As shown in Fig. 4, on these small scales there are many more ξ_- data points than ξ_+, which is exactly the opposite from the situation in the standard cosmological analysis. This is because the structure of the ξ_- kernel makes it more significantly based on small scales, and hence affected by the baryonic effects. Measurements of ξ_- thus provide particularly valuable information on the BCM parameters.

We use COSMOSIS (Zuntz et al. 2015),[2] POLYCHORD (Handley, Hobson & Lasenby 2015), CAMB (Lewis & Challinor 2011), and GETDIST (Lewis 2019) for the nested sampling and the analysis pipeline.

3.4 Systematics

Baryonic feedback is an important effect at relatively small, non-linear spatial scales, but it is by no means the *only* effect at small

scales. Hence, when using the small-scale cosmic shear measurements to constrain the baryonic effects, we need to ensure that the systematic uncertainties introduced by other small-scale effects are under control. Here, we investigate the systematics related to the intrinsic alignment and non-linear clustering. We also discuss the systematics induced by possible incorrect assumptions on the cosmological parameters, then conclude with a strategy to balance the constraining power and the bias on the baryonic parameter $\log(M_c)$.

For the investigation of several systematics that are fairly subdominant and not marginalized by modelling, we use the following strategy: we generate synthetic data vectors contaminated by certain systematics, then carry out the standard analysis by simply ignoring these systematics. We compare the posterior of M_c, the parameter that we concern the most in our analysis, between the baseline analysis and the contaminated data vector analysis. We claim that the systematics is under control when the shift in M_c is $< 0.2\sigma$.

3.4.1 Intrinsic alignments

The ellipticity of the observed galaxies is induced by either the weak lensing of the background galaxies, or else by the intrinsic alignments (IA) caused by the tidal gravitational force from cosmic structures. Intrinsic-alignment auto and cross correlations with shear are expected to have a larger effect at smaller scales. Hence we adopt a beyond-linear, perturbative-theory model to predict the intrinsic alignment in our analysis – the Tidal Alignment and Tidal Torquing (TATT) model (Blazek et al. 2019). The precise range of scales over which the TATT model is accurate is still under investigation, but here we argue that a straightforward application of TATT is sufficient for us for two reasons. First, TATT is quite flexible, as it introduces up to five nuisance parameters to capture the IA power. Second, at very small scales ($\lesssim 2$ Mpc) where TATT may start to become less accurate, the statistical errors of the DES cosmic shear measurements start to rapidly increase. Therefore, even though some non-linear IA features may not be captured by the parameter space of TATT model, they are unlikely to affect our results significantly.

With the reasoning above, we carry out our real-data analysis marginalizing over the TATT model parameters for the intrinsic alignment. After unblinding, we investigate the possible degeneracies between the IA parameters and the baryonic suppression, as discussed in Appendix B. We confirmed, based on the contours in Fig. D1, that: (1) The TATT model parameters are not correlated with M_c; (2) In our BCM analysis the constraint on the TATT parameters is consistent with DES Year-3 3x2pt and cosmic shear 1x2pt cosmological analysis results. We thus conclude that the intrinsic alignment is not biasing our baryonic physics constraints. The caveat of the above argument is that we trust the degrees of freedom introduced by TATT model to be able capture the IA features to the accuracy required by the quality of our small-scale data.

3.4.2 Non-linear matter power spectrum

In our fiducial analysis pipeline, non-linear physics is modelled by BACCOEMU. However, there still remain different choices that one can make in modelling the non-linear clustering of dark matter alone; see e.g. Martinelli et al. (2021). To address this, we ran our baseline analysis on the synthetic data vector generated by an alternative non-linear matter power spectrum model. For this alternative, we chose TAKAHASHI-HALOFIT (Takahashi et al. 2012). As shown in Fig. 2, the posteriors on $\log(M_c)$, Ω_m, and σ_8 are almost indistinguishable from the baseline case, with the tension
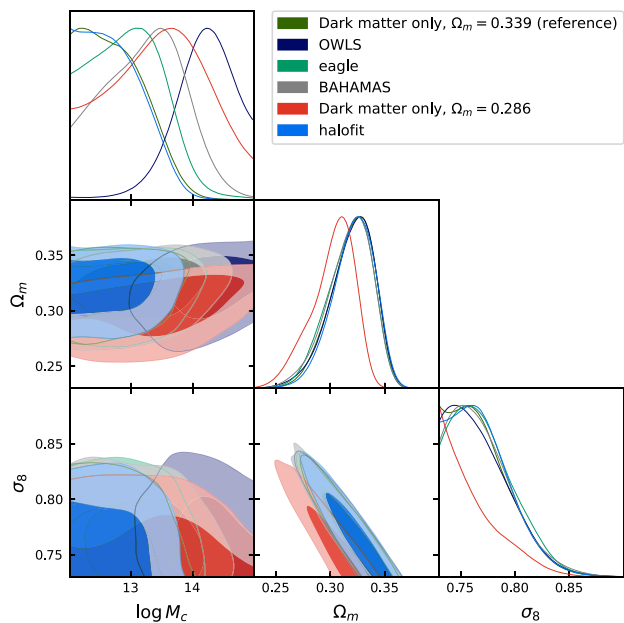
Figure 2. Test results using the baseline baryonification analysis pipeline on the synthetic data vectors. We adopt the dark-matter-only matter power spectrum (corresponding to no baryonic suppression) as our a priori fiducial reference. We then generate the matter power spectra suppressed by the redshift-dependent baryonic effect measured in OWLS-AGN (Schaye et al. 2010), BAHAMAS_T7.6_WMAP9 (McCarthy et al. 2017, 2018), and eagle (Schaye et al. 2015) simulations (Huang et al. 2019; van Daalen, McCarthy & Schaye 2020) (corresponding to decreasing amplitude of baryonic suppression). The figure shows that our analysis pipeline successfully captures the relative amplitudes of the baryonic effect between different simulations in $\log M_c$ posteriors. We also test the synthetic dark-matter-only data vector with a lower Ω_m than our parameter prior, and this leads to $\log M_c$ that is biased high, as shown in the contour labelled with $\Omega_m = 0.286$. Lastly, we replace the data-vector-generating non-linear module, switching from BACCOEMU to HALOFIT, and find that their difference is not introducing statistically significant bias in the parameter space that we are interested in.

Figure 3. Synthetic data vector tests for higher order shear effects. The DMO and OWLS contours are the same in the Fig. 2, and the two higher order shear synthetic data vectors are generated on the base of DMO and OWLS ones multiplying the ratio depicting the higher order shear effects from Fig. 5 of Secco et al. (2022). The effect of higher order shear is indicated by the deviation from green contour to grey contour, and from red contour to blue contour. In neither cases higher order shear effects cause large shift in $\log M_c$, and the shift direction is always towards smaller value of $\log M_c$, i.e. less possibility of a fake detection of the baryonic suppression.

between two posteriors being $<0.02\sigma$, so we conclude that the non-linear-modelling uncertainty will not be an issue in our analysis.

3.4.3 Cosmological model assumptions

As discussed in Section 3.2, we fix many of the cosmological parameters, a set priors on additional few, in order to focus on the constraints on the baryonic feedback. A natural concern in such an approach is the possible bias in our results introduced by incorrect assumptions on the cosmological model (relative to the ground truth, whatever it may be). To address these concerns, we perform a validation test with an alternative value of a key cosmological parameter. Specifically, we run a chain on dark-matter-only (DMO) synthetic data vector centred at the value of the matter density that is at the *lower end* of the 95 per cent credible-level constraint in the DES Year-3 3x2pt analysis. That is, given the 95 per cent C.L. DES Year-3 constraint $\Omega_m \in [0.286, 0.390]$, we adopt $\Omega_m = 0.286$, thus replacing our baseline which is the DES-Y3 central value, $\Omega_m = 0.339$. As illustrated by the red contour in Fig. 2, lower Ω_m value shifts the marginalized $\log(M_c)$ posterior away from its baseline of $\log(M_c) = 12.0$ to a higher value in the $\log(M_c) = 13.5$–14.0 range, with $\sim 0.8\sigma$ significance. Fortunately, such a scenario leaves an unambiguous additional signature, which is a shift, relative to
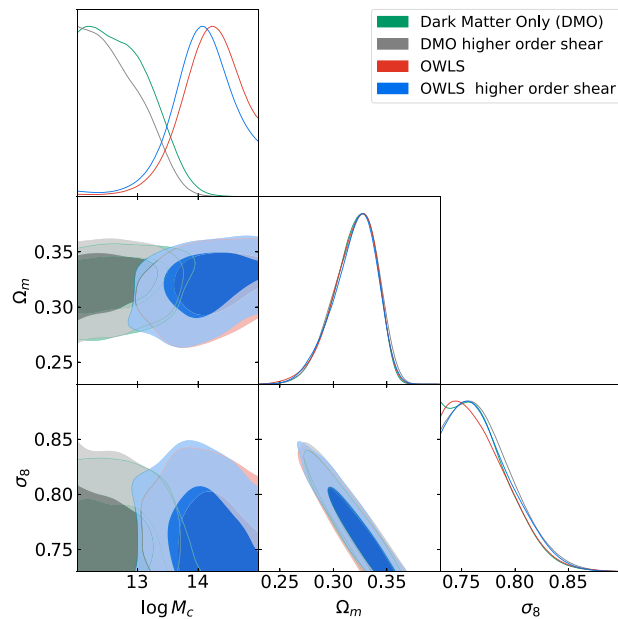
the prior, in the $\Omega_m - \sigma_8$ constraint; see the red contour relative to the others in this plane in Fig. 2. Therefore, one thing to monitor will be the comparison of the *small-scale* $\Omega_m - \sigma_8$ posterior and that obtained in the standard cosmological analysis that utilizes large scales. Any mismatch between those two may indicate a possible bias in the inferred baryonic parameter $\log(M_c)$ as well. We will see below that our analysis analysis does not show indications any such shift.

3.4.4 Higher order cosmic shear

Higher order cosmic shear corrections, including the reduced shear (Dodelson, Shapiro & White 2006) and source magnification (Schneider, Van Waerbeke & Mellier 2002), have been studied in the DES Year-3 methodology paper (Krause et al. 2021; Secco et al. 2022). As shown in fig. 5 of Secco et al. (2022), systematics due to higher order cosmic shear effects are generally subdominant to the baryonic suppression. Assuming that such effects are roughly cosmology-independent, we apply the higher order shear effects depicted by the purple dotted line in fig. 5 of Secco et al. (2022) on our DMO and OWLS synthetic data vector. The bias introduced by not including such effect in our modelling pipeline are $<0.05\sigma$ and $<0.2\sigma$ for DMO and OWLS cases as shown in Fig. 3. Hence, we conclude that higher order corrections to shear are not a concern.

3.5 Blinding

To avoid confirmation bias, we blind our results – that is, we do not reveal our principal results until we have finalized our analysis and modelling criteria and choices. Our decision to blind is motivated
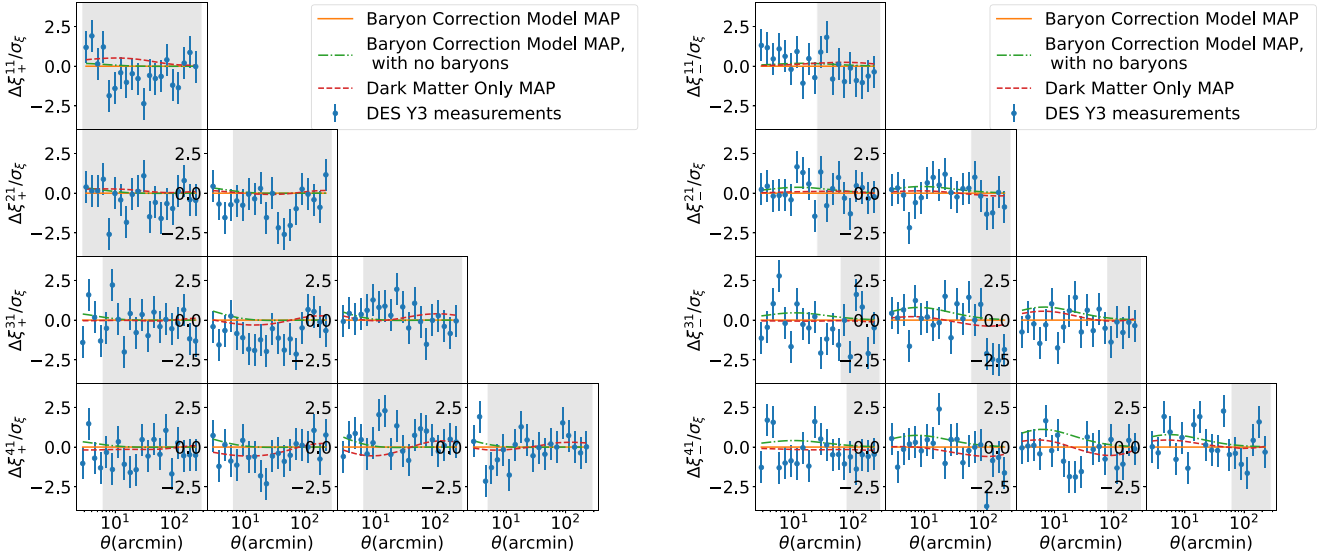
Figure 4. Tomographic cosmic-shear two-point correlation functions: ξ_+ (left panel) and ξ_- (right panel) (Amon et al. 2022). All of the curves – both theory and data – are shown relative to the best-fitting prediction under BCM, and are divided by the observational errors. The blue points are DES Year-3 measurements. The orange curves, equal to precisely zero, correspond to our best-fitting BCM model's prediction. The green curves are the predictions keeping everything the same as the orange curves, but with the baryonic suppression artificially turned off. The red dashed curves are the dark-matter-only best-fitting prediction. The grey regions show the scales *not* used in our analysis.

by the increasing realization that complex cosmological analyses require at last some level of blinding in order to prevent unintended, subjective factors in biasing the analysis results (Muir et al. 2020). Note that every aspect of our real-data analysis that leads to the results presented in Section 4 is the same as in our synthetic data tests, and that we did not alter any analysis choices after unblinding. At the same time, we must keep in mind that the DES Year-3 cosmology analysis using the large scales has already been done and is publicly available, and thus we are *not* blind to the analysis choices that have been made there and that influenced our choices in this work.

Recall, our key results will be the posteriors and other statistical measures in $\log(M_c)$, Ω_m and σ_8. It is the constraints on these parameters that we want to blind until our analysis choices have been finalized. We now summarize our blinding procedure.

Before unblinding, we calculate the posterior predictive distribution (PPD) p-value of the BCM model; for details, see Doux et al. (2021). The goal of this step is to guarantee that our model represents a reasonable description of the data. The PPD p-value characterizes the probability that the $\Delta\chi^2 = (\mathbf{D} - \mathbf{M})^{\mathrm{T}} C^{-1} (\mathbf{D} - \mathbf{M})$, evaluated between the data $\mathbf{D}$ and the theory prediction $\mathbf{M}$ for some values of the parameters, is smaller than the $\Delta\chi^2$ evaluated between a multivariate Gaussian *realization* of the data and the noiseless theory data vector. The latter quantity should obey the chi-squared distribution with the degrees of freedom equal to the number of data points, so we calculate PPD p-value as

$$p^{\mathrm{PPD}} = \sum_i \left(1 - F_{[\# \text{ of pts}]}\left(\Delta\chi_i^2\right)\right) \times w_i, \qquad (6)$$

where $F_k(x)$ is the cumulative distribution function of a chi-squared distribution with k degrees of freedom, $\Delta\chi_i^2$ is evaluated between the real data and the theory prediction at i-th sample in the MCMC chain, and w_i is the weight of the sample. The passing criterion for unblinding is $p^{\mathrm{PDD}} > 0.01$. All of our real-data chains pass this criterion; the specific values of p^{PPD} are reported in the results section below.

Having passed the PPD criterion, we also plot the maximum a posteriori (MAP) theoretical data vector from the chains with the measured data points in Fig. 4 to further confirm that the MAP of the chains reasonably captures the measurements. The cosmic shear measurements denoted by the blue dots are well within the observational uncertainty around the MAP best-fitting theory prediction of our baryonification model, denoted by the orange horizontal line.

4 RESULTS

As mentioned above, we pass the unblinding criteria that were pre-specified for our analysis. Specifically, we find a good consistency between the data and the baseline BCM (and baseline analysis choices), with PPD p-value $p = 0.50$ (see equation 6). We thus unblind the analysis at this point.

As an illustration of the suggested magnitude of the baryonic feedback on the cosmic shear two-point correlation functions, Fig. 4 shows comparison of the MAP result using theory with the BCM baseline analysis (orange; equal to precisely zero in the Figure) and theory without BCM (green), using the same parameters. The suppression of the theory with baryonic feedback – so, where orange curves are lower than green curves – is noticeable at the small scales of ξ_-, especially in the higher redshift bins. This trend can be explained by the combined effect of the increase in the ξ_- amplitude towards higher redshift, wider coverage of the lensing kernel (longer light path), and shrinking of the measurement uncertainty.

The main result is the constraint in the (Ω_m, σ_8, $\log(M_c)$) space shown in Fig. 5. We detect the $\log(M_c)$ value to be away from the lower bound of $\log(M_c) = 12.0$, which was obtained in the DMO limit. We find:

$$\log(M_c) = 14.12^{+0.62}_{-0.37} \quad 68 \text{ per cent C.L.,} \qquad (7)$$

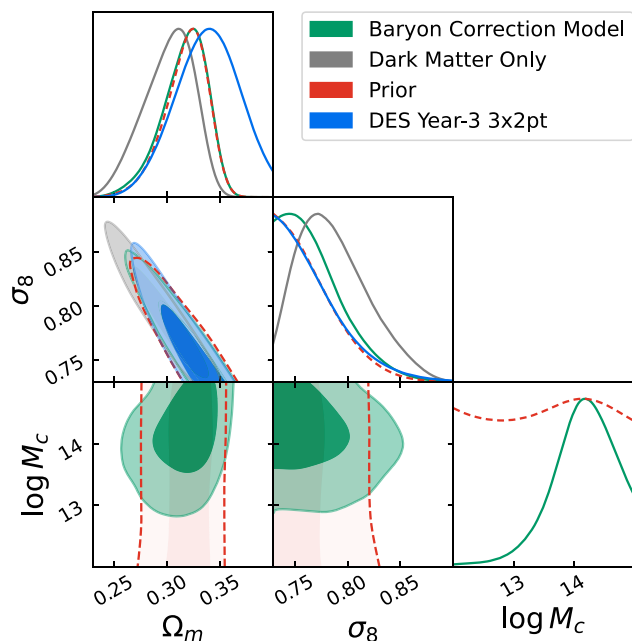$$\log(M_c) > 13.2 \quad 95 \text{ per cent C.L..} \qquad (8)$$

Figure 5. The constraints on Ω_m, σ_8, and $\log M_c$. Note that the dark-matter-only small-scale cosmic shear analysis and DES Year-3 3x2pt analysis do not have $\log M_c$ in their models. The prior in the Ω_m-σ_8 plane is taken to be the DES Year-3 3x2pt parameter posterior covariance. The shift in 1D marginalized Ω_m probability distribution in our BCM baseline away from the DES Year-3 3x2pt analysis is caused by the lower limit in σ_8 due to the limited sampling range of the emulator.

In Appendix C, we show that the effective redshift of our baryonic effect constraint is relatively low, $z_{eff} \approx 0.21$. This effective redshift is defined as the value at which our small-scale cosmic shear data vector responds most strongly to the redshift-localized BCM evaluated at that redshift. The low z_{eff} could be caused by the fact that the cosmic shear characterizes an integrated effect over the light path travelled from the source galaxy, so the effects that kick in at low redshifts are probed by multiple tomographic redshift bins. Another possibility is that the baryonic feedback is intrinsically strong at lower redshifts, but due to the integral nature of the lensing kernel, we cannot confirm this hypothesis from our analysis.

5 DISCUSSION

5.1 Model comparison with a DMO universe

The constraint on $\log(M_c)$ reported above disfavours the hypothesis of the DMO non-linear matter power spectrum. Namely, $\log(M_c) > 13.2$ suggests the presence of the baryonic suppression mode at small scales of scales probed by cosmic shear. In this section, we evaluate the statistical significance of this finding by carrying out a more detailed comparison between the cosmological models with and without baryons. In the following text, the DMO cosmology refers to a cosmology with no baryonic effect, hence all the masses are effectively dark matters which only interact through gravity. When DMO is used on a simulation, it refers to the gravity-only N-body simulations.

We calculated several popular information criteria as metrics for the model comparison in the Table 2. Their definitions are formulated in Table D1 of Appendix D. In general all the information criteria utilize the idea that the improvement in the fitting to the

measurements, i.e. the decrease of χ^2, should be punished by extra degrees of freedom of the model. Specifically, each information criterion takes a metric of the χ^2 (minimum or average), and a definition of the number of degrees of freedom, and combines them into one quantity. We use two alternate ways to measure the number of degrees of freedom k in a model: the Bayesian Model Dimensionality, BMD (Handley & Lemos 2019), and the simple counting of the free model parameters, N. The latter should provide the most conservative way of interpreting our findings, as the simple parameter count corresponds to the maximum possible number of degrees of freedom of a model. Due to the presence of priors, the effective degrees of freedom of a model k is always smaller than N. The difference in the counting of DMO and BCM model parameters, ΔN, is one, corresponding to the parameter M_c. Despite the details above, in all the statistical tests listed in Table 2, baryonification is preferred, at very strong (XIC < −3.5, where XIC stands for a certain information criterion) or moderate (−2.3 < XIC < −1.2) level as evaluated on Jeffreys' scale (Jeffreys 1961; Robert, Chopin & Rousseau 2009; Nesseris & Garcia-Bellido 2013).

We now provide estimates of the preference for the BCM. Assuming that the exponential of information criteria reflects the ratio of the two hypotheses:

(i) H0: We live in DMO universe;
(ii) H1: We live in a universe with baryons, and we need an additional parameter M_c to describe them.

We convert the probability p preferring H1 into the easy-to-gauge number of standard deviations (sigmas), z:

$$z = \sqrt{2}\, \mathrm{erf}^{-1}(p) \tag{9}$$

The bottom row of the Table 2 shows the converted number of sigmas. It shows that, in all cases, the hypothesis H1 with baryons is preferred at evidence that ranges from 1.4σ to 2.7σ.

Note that there are differences between the information criteria calculated using the BMD (Handley & Lemos 2019) and using the parameter counting N. The strong preference for the model with baryons using the BMD largely comes from this decrease of BMD in the baryon model relative to the dark-matter-only case (note the negative value in the fourth row, fourth column of Table 2). This decrease of the baryon models' degrees of freedom is counter-intuitive, because we actually *add* one degree of freedom when we go from DMO to the baryon model. The reported decrease of model dimensionality for the baryon case is likely telling us that the data fit the baryon model's features better on average. Note that BMD roughly corresponds to the variance of χ^2 for the sampled points in the chain (see the formula for BMD in Table D1). The reported decrease in BMD therefore suggests that there exists a locus in the parameter space in which the data vector prefers to settle.

5.2 Validation of the systematics

We now discuss and validate the robustness of our results to the presence of possible systematic errors and varying analysis choices.

Fig. 6 shows the marginalized constraints on M_c. The top horizontal error bar corresponds to the baseline BCM analysis, while each subsequent error bar corresponds to an analysis with one alternative analysis choice relative to the baseline, as indicated in the legend. All of the alternative results agree with the baseline results to well within statistical errors. Interpreted in the context

Table 2. Model comparison metrics between the baryonification and dark-matter-only model. We calculate Akaike Information Criterion, Bayesian Information Criterion, and Deviance Information Criterion using both the Bayesian Model Dimension (BMD) (Handley & Lemos 2019) and the naive parameter counting (N). The bottom row converts the difference in the information criteria between the BMD and DMO model into a significance for the presence of the baryonic parameter M_c quoted in 'sigmas'; see the text for details.

	$\chi^2_{\min}$	$\langle\chi^2\rangle$	BMD	N	AIC(k = BMD)	AIC(k = N)	BIC(k = BMD)	BIC(k = N)	DIC(k = BMD)	DIC(k = N)
Baryonification (BCM)	163.6	172.3	5.5	16	174.5	195.6	175.8	199.4	183.2	204.3
Dark matter only	168.4	176.2	6.0	15	179.3	197.4	180.8	200.9	188.2	206.2
BCM-DMO	−3.8	−3.9	−0.5	1	−4.8	−1.8	−5.0	−1.6	−5.0	−1.9
Significance of M_c					2.6σ	1.5σ	2.7σ	1.4σ	2.7σ	1.5σ
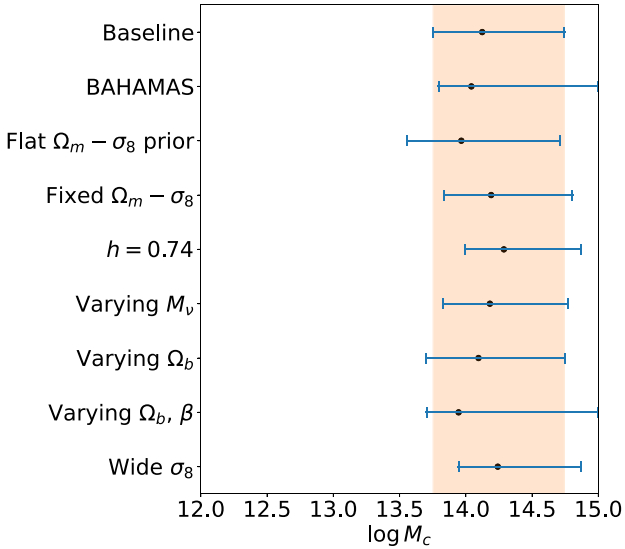
Figure 6. Systematic tests using real data. The x-axis spans the $\log M_c$ prior range. The top horizontal blue bar, which agrees with the vertical shaded region, is the marginalized 68 per cent C.L. constraint on $\log M_c$ in our baseline BCM analysis. Each subsequent horizontal error bar is the constraint on M_c from an analysis with one alternative analysis choice relative to the baseline, as indicated in the legend. The 'BAHAMAS' analysis fixes the baryonic parameters (other than $\log M_c$) to the best-fitting values in the BAHAMAS_nu0.06_Planck2015 matter power spectrum at $z = 0$ (McCarthy et al. 2017). The 'Flat Ω_m–σ_8 prior' analysis turns off the 2D Gaussian prior in the baseline analysis, varying these two parameters in the BACCOEMU range with flat priors. The 'Fixed Ω_m–σ_8' chain fixes the values of these two parameters to their DES Year-3 3x2pt means, $\Omega_m = 0.339$ and $\sigma_8 = 0.733$. The '$h = 0.74$' analysis fixes the Hubble parameter to the higher SH0ES value (Riess et al. 2019) instead of the Planck value adopted by our baseline in Table 1. The last three analyses, labelled as 'Varying (parameter name)', apply flat priors to the corresponding parameters, in the range of BACCOEMU. The 'Wide σ_8' analysis has wider σ_8 range [0.6,0.9], and uses HALOFIT to calculate the dark-matter-only non-linear power spectrum; The baryonic suppression is approximated in low-σ_8 region as $S(\sigma_8 < 0.73) = S(\sigma_8 = 0.73)$. The parameter ranges for BACCOEMU can be found at https://baccoemu.readthedocs.io/en/latest/.

of our discussion on the possible systematics in Section 3.4, we conclude:

(i) The agreement between the baseline result and the BA-HAMAS, as well as the 'Varying Ω_b, β' result justifies our assumption to fix the baryonic feedback mode (constructed by OWLS-AGN simulation at $z = 0$). In particular, our current measurement precision is not sensitive enough to distinguish this from the alternative BAHAMAS $z = 0$ baryonic feedback mode, or else from the variation

of the halo mass – gas fraction slope β. This result justifies our Fisher forecast in Section 3.1.

The slight widening of the M_c error bar is correlated with the negative β BCM parameter in the BAHAMAS best-fitting values, and the negative region allowed by the analysis varying β. The reason is that, given the gas fraction in the halo scaling as equation (A1), positive β suggests that the baryonic feedback is stronger towards less-massive haloes, and vice versa. Recall that lower f_{gas} is a signature of stronger gas ejecting processes like AGN. Since the average halo mass of the DES galaxy sample is $\sim 10^{14}\,M_\odot$ (McClintock et al. 2019), for fixed positive value of β, lower M_c ($< 10^{14}\,M_\odot$) suggest weaker baryonic feedback in the DES galaxy sample. However for a negative β value, wider M_c area in our prior range accommodates a substantial baryonic feedback for $\sim 10^{14}\,M_\odot$ population, so we get a wider error bar.

The above reasoning further supports that the halo mass population in DES galaxy sample might have witnessed a substantial baryonic feedback.

(ii) The agreement between the baseline result and the 'Flat Ω_m–σ_8', 'Fixed Ω_m–σ_8', '$h = 0.74$', and 'Varying M_ν' cases justifies our assumptions to fix the cosmological parameters. In other words, these alternatives to our baseline cosmological model do not change our constraint on the baryonic parameter M_c. It is true that we cannot explore all of the possible changes to the fiducial cosmological parameters in these limited tests, as the POLYCHORD chains would have difficulty converging with too many unconstrained cosmological parameters. However, these single-parameter-change tests, along with the Fisher PCA forecast arguments in Section 3.1, give us sufficient confidence that our detection of the baryonic feedback is not due to bias in the standard cosmological parameters.

(iii) To check if the cutting through the σ_8 range introduces any bias on the baryonic feedback constraint, we run a systematic test labelled 'Wide σ_8', where we expand the prior on σ_8 to be flat (0.6, 0.9). The challenge is how to extrapolate baryonic suppression $S(k, z)$ outside the emulator parameter space. We take the zeroth-order expansion of $S(k, z)$ in the region $\sigma_8 < 0.73$, setting $S(\sigma_8 < 0.73) = S(\sigma_8 = 0.73)$ with other cosmological and baryonic parameters unchanged. We adopt halofit to calculate the DMO non-linear matter power spectrum in this wide σ_8 range. Such an approximation of $S(k, z)$ is expected to underestimate the suppression, as $S(k, z)$ slightly increases with decreasing σ_8. So the slightly higher but consistent $\log M_c$ error bar in this test with respect to the baseline result confirms that our analysis is robust to the decision to adopt the narrower BACCOEMU σ_8 range.

(iv) We investigated our baseline posterior on the intrinsic alignment TATT model parameters, and the latter's degeneracy with M_c. The relevant constraints are shown in the Fig. D1 in Appendix B, along with the constraint on the same set of TATT parameters from the DES Year-3 cosmic shear (1x2pt) and cosmic shear combined with galaxy clustering (3x2pt) analysis. The 2D contours in TATT parameters cross M_c panels look highly uncorrelated between each

other, suggesting that the scale-dependence of the IA signal (modelled by TATT) and baryonic suppression signal is fairly distinct. Thus the possibility that the potential degeneracy with the extended intrinsic alignment degrees of freedom causing the non-trivial M_c constraint that deviates from its prior lower bound is also unlikely.

The list of systematic checks just discussed is not guaranteed to be complete. In that regard, there are several caveats in our analysis that one should keep in mind:

(i) Some systematics, for example the magnification, were argued to be small and were conventionally ignored in the previous work. However, the arguments and tests for such systematics were done at large scales that are relevant to the cosmological analysis (Krause et al. 2021). It remains to be rigorously investigated whether these assumptions still apply at smaller scales that we use here. In contrast, other systematics, such as the Limber approximation and redshift-space-distortion effects, decrease when going to smaller scales, so we should be safe from them here.

(ii) The emulator sampling is limited in the model parameter space and wavenumber space. For example, our posterior on σ_8 is cut off at 0.73 because BACCOEMU only samples down to this value. Additionally, the non-linear matter power spectrum sampling of BACCOEMU goes up to $k = 5.0\,h\,\mathrm{Mpc}^{-1}$, and beyond that wavenumber we need to extrapolate in order to compute the theory prediction for $\xi_\pm$. This limitation prevents us from modelling any enhancement of the matter power at smaller scales. We did however check, on several runs of the theory model, that including a high-k enhancement in power of roughly the expected typical magnitude only introduces a small correction to the overall baryonic-effect $\Delta\chi^2$. For example, when we change the maximum wavenumber to which the baryonic suppression is applied from $k = 5.0\,h\,\mathrm{Mpc}^{-1}$ (which is the default in our analysis and incorporates no high-k enhancement) to $k = 30.0\,h\,\mathrm{Mpc}^{-1}$ (which is realized by the direct measurements from OWLS-AGN and DMO simulations so includes the enhancement effect), the two scenarios differ by only ~ 5 per cent of the baseline $\Delta\chi^2$ difference between DMO and baryonic universe.

(iii) Baryonic feedback is a stochastic process, and in reality the baryon-corrected mass profile of haloes may vary based on a number of physical properties of the halo – the halo age, formation history, etc. The baryon-correction model might not be able to capture all these dependencies. It is possible that the simplicity of our adopted baryonic correction model biases the baryonic parameter constraints. At the same time, it is unlikely that this simplicity induces a false detection of the baryonic suppression on the matter power spectrum because the baryonic effects become negligible for the current data precision, when $M_c \to 0$.

(iv) We assume M_c to be constant with redshift. We note that X-ray observations of gas fractions in galaxy clusters are currently not accurate enough to provide a clear redshift trend (see e.g. Akino et al. 2022, and references therein), while hydrodynamical simulations predict different redshift dependences when varying subgrid physics (Aricò et al. 2020). We also notice that the drifting of best-fitting M_c in simulations, for example OWLS and BAHAMAS, is below 2σ measurement uncertainty even across a redshift range ($0.0 \lesssim z \lesssim 1.0$) much wider than what our actual data can reach (see effective redshift range in Fig. C1).

5.3 Comparison with X-ray data and previous work

The constraints on the baryonic parameters M_c and β that we have obtained can be directly translated to a prediction of the quantity of gas retained in haloes, through the Baryonic Correction Model. In
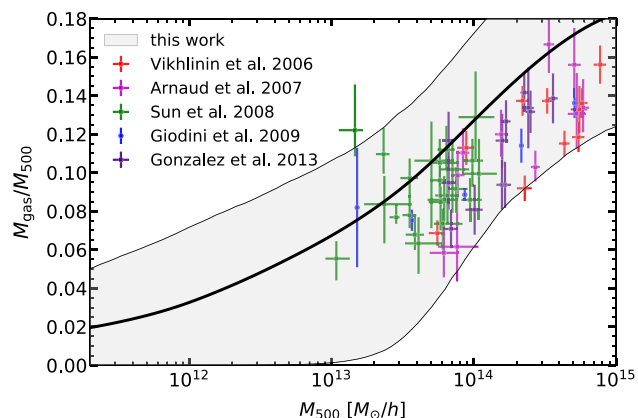

Figure 7. Gas mass fraction as a function of halo mass. The halo mass is computed assuming hydrostatic equilibrium. Data points are observations from different data sets, as reported in the legend. The grey shaded area highlights the 68 per cent credible region given by the constraints of baryonic parameters obtained in this work.

Fig. 7, we compare this prediction to observations of the gas fractions in X-ray from (Vikhlinin et al. 2006; Arnaud, Pointecouteau & Pratt 2007; Giodini et al. 2009; Sun et al. 2009; Gonzalez et al. 2013). The mass of the haloes in these observations is obtained assuming hydrostatic equilibrium, i.e. neglecting non-thermal contributions to the pressure. To fairly compare with our theoretical modelling, we rescale our halo masses by a factor $(1 + b_h)$, where b_h is the so-called hydrostatic mass bias. We assume a Gaussian distribution of b_h with mean 0.26 and standard deviation 0.07, based on Hurier & Angulo (2018). We show that the gas fractions directly observed are in good agreement with the 68 per cent credible region obtained from the cosmic shear. In particular, it appears that X-ray observations already have the potential to put tight constraints on baryonic parameters, opening up to joint constraints from lensing and X-ray, as done e.g. in Schneider et al. (2021). However, some complications may arise when joining different X-ray data sets, for instance when assessing their covariance or when marginalizing over the hydrostatic mass bias. Works such as Akino et al. (2022), which aim at building large homogeneous samples of clusters gas fractions over a wide range of halo masses, will be of great benefit in providing tighter constraints on baryonic parameters – and thus in constraining the impact of the baryons on the matter power spectrum.

In Fig. 8, we show the baryonic suppression in the power spectrum that we expect at redshift $z = 0$, given the constraints on the baryonic parameters, M_c and β, and universal baryon fraction, Ω_b/Ω_m, obtained in this work. We compare the 68 per cent credible region given by our constraints with the power spectrum suppression predicted by different hydrodynamical simulations: EAGLE, Illustris, Illustris TNG, OWLS-AGN, BAHAMAS (Schaye et al. 2010, 2015; Vogelsberger et al. 2014; McCarthy et al. 2017; Springel et al. 2018). The suppression that we find in this paper is compatible to that of the BAHAMAS simulations, particularly between their versions with the medium- and high-temperature AGN feedback, and with OWLS-AGN. Note that BAHAMAS has been calibrated with the gas mass inside galaxy groups. We have thus shown that this BAHAMAS prediction is in a very good agreement with the gas fraction implied by our small-scale cosmic shear analysis.

Our analysis, which uses the small scales of DES Year-3 cosmic shear measurements, suggests a baryonic suppression $S(k)$ of the matter power spectrum ≈ 5 per cent at $k = 1.0\,h\,\mathrm{Mpc}^{-1}$ and
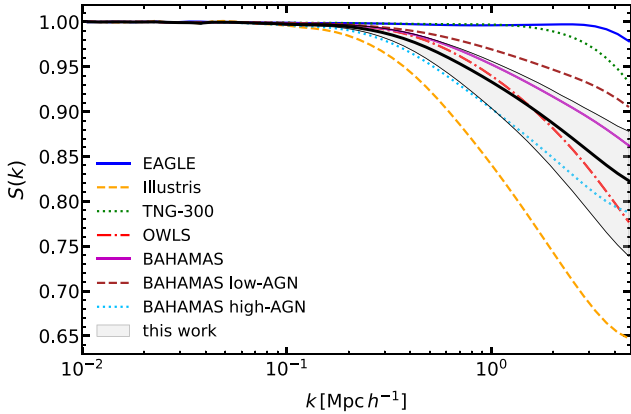
Figure 8. Suppression of the power spectrum due to baryonic effects, defined as the ratio $S(k, z = 0) = P_{\text{baryons}}/P_{\text{DMO}}$. The lines show the suppression obtained when fitting different hydrodynamical simulations with the baryonic emulator at redshift $z = 0$. The grey area highlights the 68 per cent credible region given by the constraints on the baryonic parameters obtained in this work. OWLS_AGN seems to agree the most to our best fit $S(k)$, however it should be borne in mind that we fix the baryonic parameters other than M_c to OWLS_AGN $z = 0.0$ values in our analysis.

≈ 15 per cent at $k = 5.0\,h\,\mathrm{Mpc}^{-1}$. Other previous work used weak lensing to constrain the baryonic feedback on matter power spectrum. Specifically, Huang et al. (2021) used DES Year-1 3x2pt measurements to constrain baryonic feedback using principal components of the baryonic effect signature on the power spectrum as determined by numerical simulations. Because DES Year-1 measurements are less precise than Year-3, no conclusive constraint on the baryonic feedback was drawn at the time. More recent work in Schneider et al. (2021) used KiDS-1000 (Asgari et al. 2021) as their weak lensing data set to constrain the baryonic feedback. While they could impose no informative constraint on their (seven-parameter) baryonic model, their derived effect on the matter power spectrum is broadly consistent with our results. Yoon & Jee (2021) compared the KiDS-450 measurements and the theory prediction by HMcode (Mead et al. 2016) to find a substantially stronger baryonic feedback than what we and many AGN simulations find. However they have fairly large uncertainties, and only exclude the DMO case at $\sim 1.2\sigma$. Recently, there has also been an effort in the community to measure baryonic feedback by combining weak lensing with thermal Sunyaev–Zeldovich signatures measured in CMB observations. Such an attempt with KiDS-1000 (Tröster et al. 2022) obtained baryonic constraints consistent with BAHAMAS simulation, and consequently in agreement with our findings as well. Similarly, Gatti et al. (2022a) and Pandey et al. (2022) have cross-correlated the cosmic shear measured by DES Year-3 with the Sunyaev–Zeldovich effect measured by Planck and ACT (Planck Collaboration XXII 2016; Madhavacheril et al. 2020), and modelling the signal with an hybrid approach based on hydrodynamical simulation and HMcode, finding hints of strong feedback compatible with Cosmo-OWLS high AGN (Le Brun et al. 2014), which is in broad agreement with BAHAMAS high AGN. Chen, Zhang & Yang (2022) used thermal Sunyaev–Zeldovich map from Planck around stacked DESI catalogue to explore the baryonic feedback. They found β to be always positive, which is consistent with our analysis choice of fixing $\beta = 0.321$,; their constraint on M_c also agrees with our findings.

In summary, a number of earlier analyses that constrained baryonic feedback found results that are consistent with ours.

In closing this section, we note that our results are based on a straightforward analysis that uses solely the DES Y3 cosmic shear measurements, and has been subjected to a battery of systematic tests. Because of the conservative assumptions that we made, the preference we find for the baryonic suppression, while not statistically overwhelming (at 1.4–2.7σ, depending on the assumptions), is robust.

6 CONCLUSIONS

In this paper, we constrain the effect of baryonic feedback on the matter power spectrum. As a starting point, we adopt the BCM (Schneider & Teyssier 2015; Aricò et al. 2020) which introduces seven parameters to model the baryon-corrected halo mass profile. We choose to fix all cosmological parameters except Ω_m and σ_8, and focus our attention on the baryonic sector. Specifically, we use only small angular scales in DES cosmic shear measurements to constrain the baryonic feedback. Our analysis is therefore complementary to the standard cosmological analysis that discards the small scales that we are using here, and instead uses large scales to constrain cosmology (and largely avoid the effect of baryons).

We demonstrate by means of a Fisher forecast that our DES Year-3 small-scale cosmic shear measurements are sensitive enough to constrain only one BCM parameter, $\log M_c$, where M_c is a typical mass scale related to the gas content of haloes. We also carry out a battery of tests to validate our results, specifically studying the impact of alternative assumptions in the choice of priors, parameters that are fixed or varied, and alternative models for non-linear dark-matter clustering.

We constrain the baryonic parameter $\log M_c$ to be $14.12^{+0.62}_{-0.37}$ at 68 per centC.L., while fixing other baryonic (BCM) parameters to the best fit of OWLS-AGN hydrodynamic simulation. Our analysis prefers the best-fitting baryonic model to the best-fitting DMO alternative (which corresponds to $\log M_c = 12.0$ in our analysis) at the $\sim 2\sigma$ significance.

We find good agreement between our cosmic-shear constraints on the baryonic feedback and independent X-ray measurements, as illustrated in Fig. 7. This result foreshadows exciting future possibilities: one could use independent X-ray, thermal Sunyaev–Zeldovich effect, and other observations as a prior on the baryonic-feedback parameter space, in turn enabling more precise constraints on the latter. We hope to incorporate this approach in the future, and combine it with the forthcoming DES Year-6 cosmic-shear data.

DATA AVAILABILITY

This analysis work uses DES Year-3 data release available at https://des.ncsa.illinois.edu/releases/y3a2/Y3key-products. We use only the cosmic shear two-point correlation functions, which are identical for either fits file available in the 'Data Vectors' section. We use cosmosis available at https://github.com/joezuntz/cosmosis as our cosmology likelihood sampling software. We use Baccoemu available at https://pypi.org/project/baccoemu/ to produce linear, non-linear and baryon-corrected matter power spectrum.

REFERENCES

Abbott T. et al., 2022, Phys. Rev. D, 105, 023520
Akino D. et al., 2022, PASJ, 74, 175
Amon A. et al., 2022, Phys. Rev. D, 105, 023514
Angulo R. E., White S. D. M., 2010, MNRAS, 405, 143
Angulo R. E., Zennaro M., Contreras S., Aricò G., Pellejero-Ibañez M., Stücker J., 2021, MNRAS, 507, 5869
Aricò G., Angulo R. E., Hernández-Monteagudo C., Contreras S., Zennaro M., Pellejero-Ibañez M., Rosas-Guevara Y., 2020, MNRAS, 495, 4800
Aricò G., Angulo R. E., Zennaro M., 2021a, preprint (arXiv:2104.14568)
Aricò G., Angulo R. E., Hernández-Monteagudo C., Contreras S., Zennaro M., 2021b, MNRAS, 503, 3596
Aricò G., Angulo R. E., Contreras S., Ondaro-Mallea L., Pellejero-Ibañez M., Zennaro M., 2021c, MNRAS, 506, 4070
Arnaud M., Pointecouteau E., Pratt G. W., 2007, A&A, 474, L37
Asgari M. et al., 2021, A&A, 645, A104
Blazek J., MacCrann N., Troxel M. A., Fang X., 2019, Phys. Rev. D, 100, 103506
Chen Z., Zhang P., Yang X., 2022, preprint (arXiv:2201.12591)
Contreras S., Angulo R. E., Zennaro M., Aricò G., Pellejero-Ibañez M., 2020, MNRAS, 499, 4905
Dodelson S., Shapiro C., White M. J., 2006, Phys. Rev. D, 73, 023009
Doux C. et al., 2021, MNRAS, 503, 2688
Eifler T. et al., 2021, MNRAS, 507, 1514
Fagrelius P. A., 2020, in American Astronomical Society Meeting Abstracts #235. p. 446.01
Gatti M. et al., 2021, MNRAS, 504, 4312
Gatti M. et al., 2022a, Phys. Rev. D, 105, 123525
Gatti M. et al., 2022b, MNRAS, 510, 1223
Giodini S. et al., 2009, ApJ, 703, 982
Giri S. K., Schneider A., 2021, J. Cosmol. Astropart. Phys., 12, 046
Gonzalez A. H., Sivanandam S., Zabludoff A. I., Zaritsky D., 2013, ApJ, 778, 14
Handley W., Lemos P., 2019, Phys. Rev. D, 100, 023512
Handley W., Hobson M., Lasenby A., 2015, MNRAS, 450, L61
Huang H.-J., Eifler T., Mandelbaum R., Dodelson S., 2019, MNRAS, 488, 1652
Huang H.-J. et al., 2021, MNRAS, 502, 6010
Hurier G., Angulo R. E., 2018, A&A, 610, L4
Jeffreys H., 1961, Theory of Probability. Clarendon Press, Oxford
Krause E. et al., 2021, preprint (arXiv:2105.13548)
Le Brun A. M. C., McCarthy I. G., Schaye J., Ponman T. J., 2014, MNRAS, 441, 1270
Lee M. E., Lu T., Haiman Z., Liu J., Osato K., 2022, preprint (arXiv:2201.08320)
Lesgourgues J., 2011, preprint (arXiv:1104.2932)
Lewis A., 2019, preprint (arXiv:1910.13970)
Lewis A., Challinor A., 2011, Astrophysics Source Code Library, record ascl: 1102
MacCrann N. et al., 2016, MNRAS, 465, 2567
Madhavacheril M. S. et al., 2020, Phys. Rev. D, 102, 023534
Martinelli M. et al., 2021, A&A, 649, A100
McCarthy I. G., Schaye J., Bird S., Le Brun A. M. C., 2017, MNRAS, 465, 2936
McCarthy I. G., Bird S., Schaye J., Harnois-Deraps J., Font A. S., Van Waerbeke L., 2018, MNRAS, 476, 2999
McClintock T. et al., 2019, MNRAS, 482, 1352
Mead A., Heymans C., Lombriser L., Peacock J., Steele O., Winther H., 2016, MNRAS, 459, 1468
Mead A., Brieden S., Tröster T., Heymans C., 2021, MNRAS, 502, 1401
Muir J. et al., 2020, MNRAS, 494, 4454
Nesseris S., Garcia-Bellido J., 2013, J. Cosmol. Astropart. Phys., 2013, 036
Nicola A. et al., 2022, J. Cosmol. Astropart. Phys., 2022, 046
Pandey S. et al., 2022, Phys. Rev. D, 105, 123526
Planck Collaboration XXII, 2016, A&A, 594, A22
Planck Collaboration VI, 2020, A&A, 641, A6
Riess A. G., Casertano S., Yuan W., Macri L. M., Scolnic D., 2019, ApJ, 876, 85
Robert C. P., Chopin N., Rousseau J., 2009, Stat. Sci., 24, 141
Schaye J. et al., 2010, MNRAS, 402, 1536
Schaye J. et al., 2015, MNRAS, 446, 521
Schneider A., Teyssier R., 2015, J. Cosmology Astropart. Phys., 12, 049
Schneider P., Van Waerbeke L., Mellier Y., 2002, A&A, 389, 729
Schneider A., Giri S. K., Amodeo S., Refregier A., 2022, MNRAS, 514, 3802
Secco L. F. et al., 2022, Phys. Rev. D, 105, 023515

Sevilla-Noarbe I. et al., 2021, ApJS, 254, 24

Sheldon E. S., Becker M. R., MacCrann N., Jarvis M., 2020, ApJ, 902, 138

Springel V. et al., 2018, MNRAS, 475, 676

Sun M., Voit G. M., Donahue M., Jones C., Forman W., Vikhlinin A., 2009, ApJ, 693, 1142

Takada M. et al., 2014, PASJ, 66, R1

Takahashi R., Sato M., Nishimichi T., Taruya A., Oguri M., 2012, ApJ, 761, 152

Thiele L. et al., 2022, Phys. Rev. D, 105, 083505

Tröster T. et al., 2022, A&A, 660, A27

van Daalen M. P., McCarthy I. G., Schaye J., 2020, MNRAS, 491, 2424

Vikhlinin A., Kravtsov A., Forman W., Jones C., Markevitch M., Murray S. S., Van Speybroeck L., 2006, ApJ, 640, 691

Vogelsberger M. et al., 2014, MNRAS, 444, 1518

Yoon M., Jee M. J., 2021, ApJ, 908, 13

Zennaro M., Angulo R. E., Aricò G., Contreras S., Pellejero-Ibáñez M., 2019, MNRAS, 489, 5938

Zuntz J. et al., 2015, Astron. Comput., 12, 45

APPENDIX A: BARYON CORRECTION MODEL

The BCM, also known as *baryonification* (Schneider & Teyssier 2015; Aricò et al. 2020), is a scheme to perturb the output of *N*-body simulations to include given baryon processes. Each halo in the simulation is decomposed into a dark matter and baryonic component with a respective density profile associated. The difference between the profiles is then used to compute a displacement field that is applied to the particles of the halo. The functional forms of the density profiles are motivated by observations, theoretical arguments, and hydrodynamical simulations, and they depend on a few free parameters.

The scheme we use in this work decomposes the halo in dark matter, gas, and galaxies (Aricò et al. 2021b). The gas can be bound to its halo in hydrostatic equilibrium, ejected by some feedback process, or reaccreted, whereas the galaxies can be central or satellites. The baryonic gravitational potential backreacts on to the dark matter, causing a quasi-adiabatically relaxation. The evaluation of the baryonic effects on the power spectrum are speed up using a neural network emulator (Aricò et al. 2021c). This model has a total of seven free parameters, but in Section 3.1 we show that our data are mostly sensitive to one parameter, namely, M_c. This parameter regulates the amount of gas that is retained in haloes, f_{gas}, and therefore also the quantity of gas ejected by baryonic feedback, through the equation

$$f_{gas} = \frac{\Omega_b/\Omega_m - f_{gal}}{1 + (M_c/M_{200})^\beta}, \qquad (A1)$$

where f_{gal} is the mass fraction of galaxies, M_{200} is the total mass of the halo, and β another free parameter. Therefore, M_c is defined as the characteristic halo mass for which half of the halo gas is depleted.

The parameters θ_{inn}, θ_{out}, and M_{inn} regulate the density of the hydrostatic gas in the halo, according to a double power-law shape. The parameter η set the maximum distance from the halo that the ejected gas can reach, in units of the halo escape radius. Finally, $M_{z0, cen}$ regulates the characteristic galaxy mass fraction following an abundance-matching scheme. We refer to Aricò et al. (2020, 2021b) for the complete equations and baryonic functional forms of the BCM employed.

In this work, we fix all the parameters except M_c to the best-fitting values obtained fitting the OWLS-AGN hydrodynamical simulation in Aricò et al. (2021c).

APPENDIX B: INTRINSIC ALIGNMENT PARAMETERS

The measurement of the averaged cosmic shears is based on the directly obtained ellipticities of the galaxies. However, because the galaxies are formed in the gravitational field of the large-scale structures, they have non-spherically randomly distributed shapes (intrinsic alignments) under the effect of tidal forces. The intrinsic alignment is another major source of astrophysical systematics at small scales of the cosmic shear measurement, other than the baryonic suppression we are studying in this work. Hence, we are obliged to investigate whether any IA signals would be degenerate with the baryonic suppression, thus resulting in a fake detection of the baryonic suppression. Although a reliable modelling of the IA terms at small scale is not currently available to the best of our knowledge, Fig. D1 indicate two facts: (1) There is no strong correlation between baryonic parameter M_c and IA-TATT parameters $A_1 A_2$, A_1/A_2, α_1, α_2 and bias$_{ta}$; (2) The IA-TATT model (Blazek et al. 2019) parameters constraints for our baseline analysis using only the small scales of the cosmic shear are consistent with DES Year-3 large-scale cosmic shear 1x2pt and cosmic shear + clustering 3x2pt analysis.

Given the M_c-IA parameters contour plots, we conclude that the IA signal is not substantially correlated with the baryonic suppression pattern, so will not introduce significant systematics to our baryonic constraints. What is more, by comparing with other constraints on the IA parameters from DES Year-3 1x2pt and 3x2pt analysis, the consistent IA results show that there is indeed no unexpected IA signal in our small-scale cosmic shear analysis.

APPENDIX C: EFFECTIVE REDSHIFT OF THE BCM CONSTRAINT

As a photometric survey, DES galaxy catalogues do not have high-precision measurements on the redshifts, so the astrophysical and cosmological findings usually contain information blending in a range of redshifts. However, in Section 4, we provide the effective redshift at which our constraint on M_c is attached to. In this section, we explain how we get this number $z_{eff} = 0.21$.

The strategy is based on the following reasoning: the redshift-localized baryonic suppression effect that makes the most difference in the statistics (likelihood, or χ^2) is the redshift our measurement

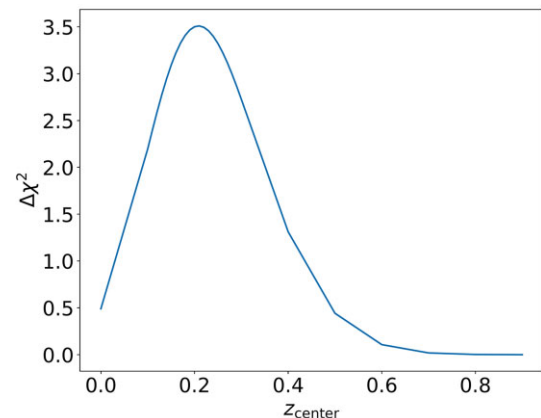**Figure C1.** To find the effective redshift in our data that are most sensitive to the baryonic suppression signal, we restrain BCM $S(k, z)$ with a Gaussian kernel around the centre redshift ($S(k, z) \to 1.0$ away from the centre redshift). The figure shows the $\Delta\chi^2$ between redshift-localized BCM and DMO data vectors. The Gaussian kernels used in this figure have $\sigma_z = 0.1$.

most sensitive to, in terms of the baryonic suppression effect constraints. So we apply a Gaussian kernel with width $\sigma_z = 0.1$ on the baryonic suppression $S(k, z)$ modelled by `Baccoemu`. At the centre redshift, BCM $S(k, z)$ is multiplied to the DMO matter power spectrum, while away from the Gaussian kernel centre $S(k, z) \rightarrow 1$. Scanning z_{centre} through from 0.0 to 1.0, we find the $\Delta\chi^2$ between redshift-localized BCM and DMO data vector peaks at 0.21. Thus we conclude $z_{\text{eff}} = 0.21$ is the effective redshift contributing the most to our baryonic feedback constraining power.

APPENDIX D: INFORMATION CRITERIA DEFINITIONS

It is a inclusive debate that which information criterion serves the best (unbiased and statistically significant) for the purpose of model comparison in cosmology. However, if a finding is significant enough, we believe it should show up regardless of the metric, so we present all the popular metrics in the result section for readers to choose their favourite. Table D1 gives the unambiguous definitions of the information criteria we presented in the main text.
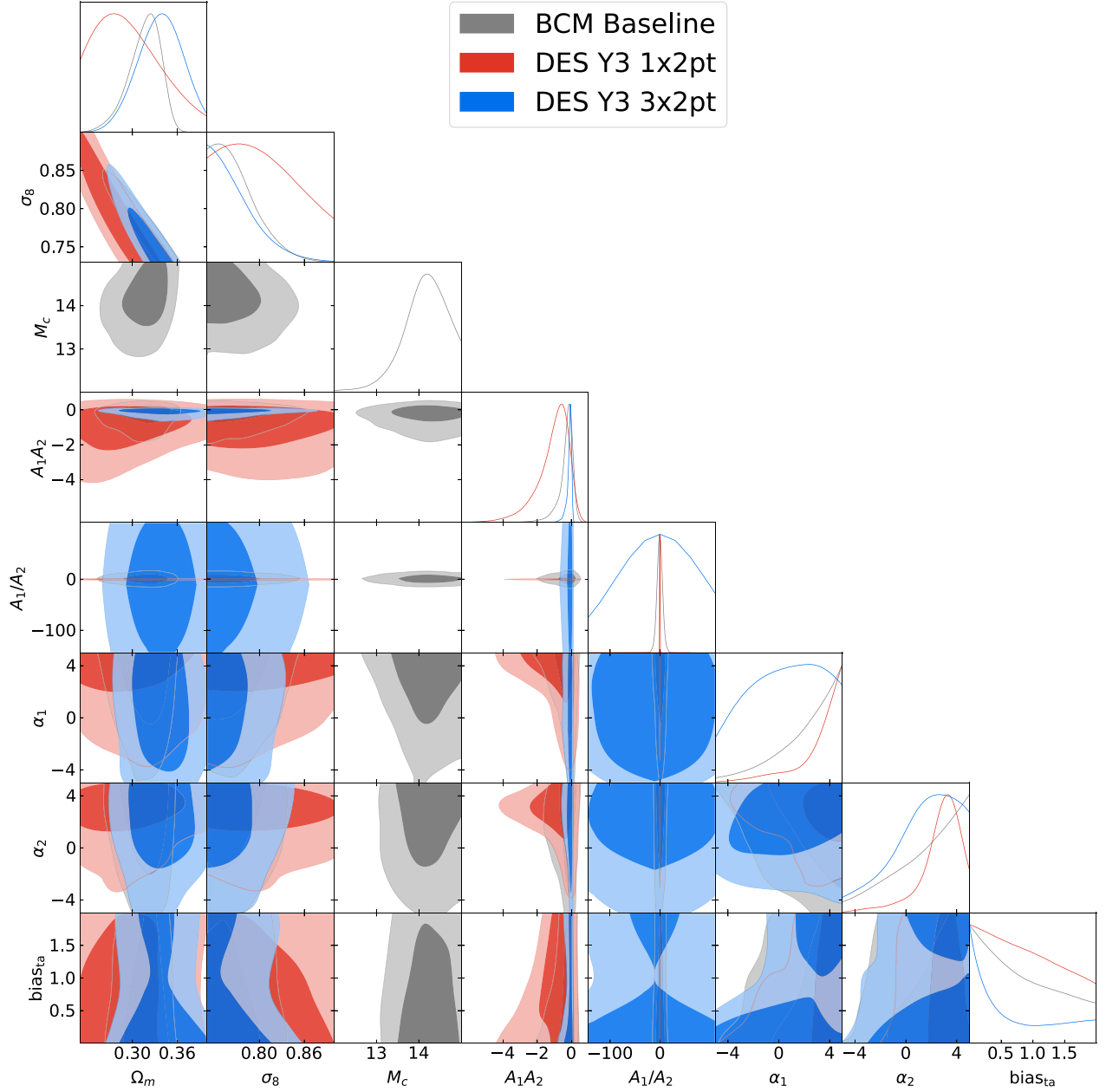

Figure D1. Contour plots for Ω_m, σ_8, and M_c, from BCM baseline analysis MCMC chain and DES Year-3 1x2pt and 3x2pt (Abbott et al. 2022) MCMC chains.

Table D1. Information Criteria Definitions. Our data **D** consist of the small-scale cosmic shear $\xi_{\pm}$ measurements from DES Year-3, with the number of data points $N_{pts} = 173$. All averages are done by integrating the posterior, namely, the average by weight of the Monte Carlo chain.

Name of the quantity	Formula
χ^2	$(\mathbf{M} - \mathbf{D})^T C^{-1} (\mathbf{M} - \mathbf{D})$
BMD	$\langle (-\frac{\chi^2}{2} - \mathcal{Z})^2 \rangle - \langle -\frac{\chi^2}{2} - \mathcal{Z} \rangle^2$
	$\mathcal{Z}$ being the logarithm evidence
AIC	$\chi^2_{min} + 2 * BMD$
AIC$(k = N)$	$\chi^2_{min} + 2 * N_{model}$
BIC	$\chi^2_{min} + BMD * \log(N_{pts})$
BIC$(k = N)$	$\chi^2_{min} + N_{model} * \log(N_{pts})$
DIC	$\langle \chi^2 \rangle + 2*BMD$
DIC$(k = N)$	$\langle \chi^2 \rangle + 2*N_{model}$

[1]*Department of Physics, University of Michigan, Ann Arbor, MI 48109, USA*

[2]*Kavli Institute for the Physics and Mathematics of the Universe (WPI), UTIAS, The University of Tokyo, Kashiwa, Chiba 277-8583, Japan*

[3]*Institute for Computational Science, University of Zurich, Winterthurerstrasse 190, CH-8057 Zurich, Switzerland*

[4]*Donostia International Physics Center (DIPC), Paseo Manuel de Lardizabal, 4, E-20018 Donostia-San Sebastián, Guipuzkoa, Spain*

[5]*Departamento de Física, Universidad de Zaragoza, Pedro Cerbuna 12, E-50009 Zaragoza, Spain*

[6]*IKERBASQUE, Basque Foundation for Science, E-48013, Bilbao, Spain*

[7]*Lawrence Berkeley National Laboratory, 1 Cyclotron Road, Berkeley, CA 94720, USA*

[8]*Kavli Institute for Cosmology, University of Cambridge, Madingley Road, Cambridge CB3 0HA, UK*

[9]*Kavli Institute for Cosmological Physics, University of Chicago, Chicago, IL 60637, USA*

[10]*Department of Astrophysics Research, Instituto de Astrofísica de Canarias, CVía Láctea, sn, E-38205 La Laguna, Tenerife, Spain*

[11]*Departamento de Astrofísica, Universidad de La Laguna, Avenida Francisco Sánchez, sn, E-38205 La Laguna, Tenerife, Spain*

[12]*Argonne National Laboratory, 9700 South Cass Avenue, Lemont, IL 60439, USA*

[13]*Laboratório Interinstitucional de e-Astronomia - LIneA, Rua Gal. José Cristino 77, Rio de Janeiro, RJ 20921-400, Brazil*

[14]*Kavli Institute for Particle Astrophysics & Cosmology, PO Box 2450, Stanford University, Stanford, CA 94305, USA*

[15]*Institute for Astronomy, University of Hawai'i, 2680 Woodlawn Drive, Honolulu, HI 96822, USA*

[16]*Physics Department, 2320 Chamberlin Hall, University of Wisconsin-Madison, 1150 University Avenue Madison, WI 53706-1390, USA*

[17]*Department of Physics and Astronomy, University of Pennsylvania, Philadelphia, PA 19104, USA*

[18]*Department of Physics, Northeastern University, Boston, MA 02115, USA*

[19]*Laboratory of Astrophysics, École Polytechnique Fédérale de Lausanne (EPFL), Observatoire de Sauverny, CH-1290 Versoix, Switzerland*

[20]*Instituto de Física Gleb Wataghin, Universidade Estadual de Campinas, Campinas, SP 13083-859, Brazil*

[21]*Jodrell Bank Center for Astrophysics, School of Physics and Astronomy, University of Manchester, Oxford Road, Manchester M13 9PL, UK*

[22]*Instituto de Física Teórica, Universidade Estadual Paulista, São Paulo, SP 01140-070, Brazil*

[23]*Department of Physics, Carnegie Mellon University, Pittsburgh, PA 15312, USA*

[24]*Instituto de Astrofisica de Canarias, E-38205 La Laguna, Tenerife, Spain*

[25]*Universidad de La Laguna, Dpto. Astrofísica, E-38206 La Laguna, Tenerife, Spain*

[26]*Center for Astrophysical Surveys, National Center for Supercomputing Applications, 1205 West Clark St., Urbana, IL 61801, USA*

[27]*Department of Astronomy, University of Illinois at Urbana-Champaign, 1002 W. Green Street, Urbana, IL 61801, USA*

[28]*Physics Department, William Jewell College, Liberty, MO 64068, USA*

[29]*Department of Astronomy and Astrophysics, University of Chicago, Chicago, IL 60637, USA*

[30]*Department of Physics, Duke University, Durham, NC 27708, USA*

[31]*Fermi National Accelerator Laboratory, PO Box 500, Batavia, IL 60510, USA*

[32]*Center for Cosmology and Astro-Particle Physics, The Ohio State University, 191 West Woodruff Avenue, Columbus, OH 43210, USA*

[33]*Department of Physics, The Ohio State University, 191 West Woodruff Avenue, Columbus, OH 43210, USA.*

[34]*Institut d'Estudis Espacials de Catalunya (IEEC), E-08034 Barcelona, Spain*

[35]*Institute of Space Sciences (ICE, CSIC), Campus UAB, Carrer de Can Magrans, s/n, E-08193 Barcelona, Spain*

[36]*Hamburger Sternwarte, Universität Hamburg, Gojenbergsweg 112, D-21029 Hamburg, Germany*

[37]*NSF AI Planning Institute for Physics of the Future, Carnegie Mellon University, Pittsburgh, PA 15213, USA*

[38]*The Warren Center for Network & Data Sciences, 3401 Walnut Street, 4th floor BC wings Philadelphia, PA 19104, USA*

[39]*Department of Astronomy/Steward Observatory, University of Arizona, 933 North Cherry Avenue, Tucson, AZ 85721-0065, USA*

[40]*Jet Propulsion Laboratory, California Institute of Technology, 4800 Oak Grove Dr., Pasadena, CA 91109, USA*

[41]*Department of Physics & Astronomy, University College London, Gower Street, London WC1E 6BT, UK*

[42]*Center for Cosmology and Astro-Particle Physics, The Ohio State University, Columbus, OH 43210, USA*

[43]*Department of Physics, The Ohio State University, Columbus, OH 43210, USA*

[44]*Department of Astronomy, University of California, Berkeley, 501 Campbell Hall, Berkeley, CA 94720, USA*

[45]*Institut de Física d'Altes Energies (IFAE), The Barcelona Institute of Science and Technology, Campus UAB, E-08193 Bellaterra (Barcelona), Spain*

[46]*Department of Physics, Ludwig-Maximilians-Universitat, Scheinerstr. 1, D-81679 München, Germany*

[47]*Department of Physics, University of Oxford, Denys Wilkinson Building, Keble Road, Oxford OX1 3RH, UK*

[48]*School of Physics and Astronomy, Cardiff University, Cardiff CF24 3AA, UK*

[49]*Department of Astronomy, University of Geneva, ch. d'Écogia 16, CH-1290 Versoix, Switzerland*

[50]*Department of Physics, University of Arizona, Tucson, AZ 85721, USA*

[51]*Laboratoire de Physique de l'Ecole Normale Supérieure, ENS, Université PSL, CNRS, Sorbonne Université, Université de Paris, F-75005 Paris, France*

[52]*Department of Physics, ETH Zurich, Wolfgang-Pauli-Strasse 16, CH-8093 Zurich, Switzerland*

[53]*Department of Physics and Astronomy, Pevensey Building, University of Sussex, Brighton BN1 9QH, UK*

[54]*Instituto de Astrofísica e Ciências do Espaço, Faculdade de Ciências, Universidade de Lisboa, P-1769-016 Lisboa, Portugal*

[55]*Department of Applied Mathematics and Theoretical Physics, University of Cambridge, Cambridge CB3 0WA, UK*

[56]*Perimeter Institute for Theoretical Physics, 31 Caroline St. North, Waterloo, ON N2L 2Y5, Canada*

[57]*Department of Physics, Stanford University, 382 Via Pueblo Mall, Stanford, CA 94305, USA*

[58]*SLAC National Accelerator Laboratory, Menlo Park, CA 94025, USA*

[59]*ICTP South American Institute for Fundamental Research, Instituto de Física Teórica, Universidade Estadual Paulista, São Paulo, SP 01140-070, Brazil*

[60]*Centro de Investigaciones Energéticas, Medioambientales y Tecnológicas (CIEMAT), Madrid E-28040, Spain*

[61]*Brookhaven National Laboratory, Bldg 510, Upton, NY 11973, USA*

[62]*Department of Physics and Astronomy, Stony Brook University, Stony Brook, NY 11794, USA*

[63]*Département de Physique Théorique and Center for Astroparticle Physics, Université de Genève, 24 quai Ernest Ansermet, CH-1211 Geneva, Switzerland*

[64]*Excellence Cluster Origins, Boltzmannstr 2, D-85748 Garching, Germany*

[65]*Max Planck Institute for Extraterrestrial Physics, Giessenbachstrasse, D-85748 Garching, Germany*

[66]*Universitäts-Sternwarte, Fakultät für Physik, Ludwig-Maximilians Universität München, Scheinerstr 1, D-81679 München, Germany*

[67]*George P. and Cynthia Woods Mitchell Institute for Fundamental Physics and Astronomy, and Department of Physics and Astronomy, Texas A&M University, College Station, TX 77843, USA*

[68]*Institute for Astronomy, University of Edinburgh, Edinburgh EH9 3HJ, UK*

[69]*Institute of Cosmology and Gravitation, University of Portsmouth, Portsmouth PO1 3FX, UK*

[70]*CNRS, UMR 7095, Institut d'Astrophysique de Paris, F-75014 Paris, France*

[71]*Institut d'Astrophysique de Paris, Sorbonne Universités, UPMC Univ Paris 06, UMR 7095, F-75014 Paris, France*

[72]*School of Physics and Astronomy, University of Nottingham, Nottingham NG7 2RD, UK*

[73]*Astronomy Unit, Department of Physics, University of Trieste, via Tiepolo 11, I-34131 Trieste, Italy*

[74]*INAF-Osservatorio Astronomico di Trieste, via G. B. Tiepolo 11, I-34143 Trieste, Italy*

[75]*Institute for Fundamental Physics of the Universe, Via Beirut 2, I-34014 Trieste, Italy*

[76]*Department of Physics, IIT Hyderabad, Kandi, Telangana 502285, India*

[77]*Institute of Theoretical Astrophysics, University of Oslo, PO Box 1029 Blindern, NO-0315 Oslo, Norway*

[78]*Instituto de Fisica Teorica UAM/CSIC, Universidad Autonoma de Madrid, E-28049 Madrid, Spain*

[79]*Department of Astronomy, University of Michigan, Ann Arbor, MI 48109, USA*

[80]*Institute of Astronomy, University of Cambridge, Madingley Road, Cambridge CB3 0HA, UK*

[81]*Observatório Nacional, Rua Gal. José Cristino 77, Rio de Janeiro, RJ 20921-400, Brazil*

[82]*School of Mathematics and Physics, University of Queensland, Brisbane, QLD 4072, Australia*

[83]*Santa Cruz Institute for Particle Physics, Santa Cruz, CA 95064, USA*

[84]*Center for Astrophysics | Harvard & Smithsonian, 60 Garden Street, Cambridge, MA 02138, USA*

[85]*Australian Astronomical Optics, Macquarie University, North Ryde, NSW 2113, Australia*

[86]*Lowell Observatory, 1400 Mars Hill Rd, Flagstaff, AZ 86001, USA*

[87]*Department of Astrophysical Sciences, Princeton University, Peyton Hall, Princeton, NJ 08544, USA*

[88]*Institució Catalana de Recerca i Estudis Avançats, E-08010 Barcelona, Spain*

[89]*School of Physics and Astronomy, University of Southampton, Southampton, SO17 1BJ, UK*

[90]*Computer Science and Mathematics Division, Oak Ridge National Laboratory, Oak Ridge, TN 37831, USA*

This paper has been typeset from a TeX/LaTeX file prepared by the author.